Original Research

A FRAMEWORK FOR SIMULATING THE PARTIALLY MISCIBLE MULTI-COMPONENT HYDROCARBON FLUIDS IN POROUS MEDIA VIA THE PSEUDO-POTENTIAL LATTICE BOLTZMANN MODEL

Zhicheng W. Wang[1], Cheng Peng[2], Luis F. Ayala[3], Seyyed A. Hosseini[1]

[1]Bureau of Economic Geology, The University of Texas at Austin, Austin, TX, USA; [2]School of Mechanical Engineering, Shandong University, Jinan, Shandong Province, China; [3]Department of Energy and Mineral Engineering, The Pennsylvania State University, University Park, PA; USA

Correspondence to:
Zhicheng W. Wang at zhicheng.wang@beg.utexas.edu

How to Cite:
Wang, Z. W., Peng, C., Ayala, L., & Hosseini, S. (2024). A framework for simulating the partially miscible multi-component hydrocarbon fluids in porous media via the pseudo-potential lattice Boltzmann model. *InterPore Journal*, *1*(1), ipj260424–5. https://doi.org/10.69631/ipj.v1i1nr7

RECEIVED: 31 Oct. 2023
ACCEPTED: 11 Mar. 2024
PUBLISHED: 26 Apr. 2024

ABSTRACT

Retrograde condensation is a unique pressure-volume-temperature (PVT) behavior of partially multi-component hydrocarbon mixtures in porous media. However, some important physical properties, such as the component composition in each phase, the surface tension of the mixture, and the fluid wettability on specific rock surfaces at given temperatures, pressures, and molar compositions are difficult to evaluate dynamically in a laboratory. Previously, a multicomponent multiphase (MCMP) model was proposed to simulate the behavior of fluids composed of multiple components, such as gas condensate fluids or volatile oil fluids, where the components are partially miscible with each other. In this study, we extend the previously developed MCMP lattice Boltzmann (LB) model for partially miscible fluids by proposing a new framework to investigate the fluids' phase behavior and flow dynamics under different phase conditions in porous media. The proposed framework integrates multiple lattice Boltzmann models to enable the convenient generation of desired wettability conditions on structural surfaces. A porous medium generated by the Voronoi tessellation (VT) was used in the case study to represent the pore-scale environment. The consistent scaling system in LB simulations was also briefly discussed. The proposed framework can enhance the understanding of the behavior of these fluids under varying conditions and can provide valuable insights into the qualitative evaluation of the pore-scale multiphase flow mechanism. Overall, this work contributes to the development of a computational framework for studying partially miscible hydrocarbon mixtures, which has important implications for the oil and gas industry.

KEYWORDS

Retrograde condensation, Multicomponent multiphase fluid, Pseudo-potential lattice Boltzmann models, Partially miscible

1. INTRODUCTION

Retrograde condensation is a unique thermodynamic behavior of lattice Boltzmann (LB) multicomponent (MC) mixtures, such as hydrocarbon mixtures, which are widely present in oil and natural gas reservoirs. It occurs when the in-situ gas is compressed beyond the dew point, with the effect that liquid condenses once the pressure drops below the dew point. The retrograde condensation phenomenon has been observed in various oil and gas fields globally, including notable examples such as the Marcellus shale in the US, the Ekofisk field in the North Sea, and the Ghawar field in Saudi Arabia. According to the US Energy Information Administration (EIA) (9), the annual production of condensate reaches an impressive 1.7 million barrels per day in 2021, highlighting the significant impact and scale of retrograde condensate production in the industry.

The envelope in a pressure–temperature (P-T) diagram to depict the two-phase region of an MC hydrocarbon mixture with a given composition is referred to as a ‘phase envelope’ (7). Inside a phase, the envelope is the region of P-T conditions under which a fluid separates into two phases. Unlike pure substances, where liquid-vapor coexistence can only occur under a specific pressure at a given temperature, MC mixtures can have two-phase coexistence under a range of pressures and remain in equilibrium. Both phases may contain all components, but their molar compositions are distinct from the particular phases. In each phase, all components are fully miscible and form a homogeneous mixture, and different phases are immiscible with each other to form an interface. Component mass transfer may occur when P–T conditions change. This type of hydrocarbon mixture is referred to as partially miscible fluid.

Retrograde condensation in porous media has been extensively studied using various methods, including early theoretical (32) and experimental research (13). Recently, researchers have explored its mechanism using phase equilibrium models (27) and have conducted simulations using molecular dynamics (MD) (37). However, studying retrograde condensation in porous media can present challenges, whether theoretically or experimentally. Theoretical studies often rely on simplified assumptions regarding fluid properties or the environment, which can limit the accuracy and applicability of the mathematical models. Experimental studies, on the other hand, face obstacles, such as real-time measurement of porous media properties and visualization of the dynamics during experiments. Retrograde condensation occurs within the pores of a porous medium, making direct observation difficult. Additionally, experimental studies can be time-consuming and resource-intensive, even with the aid of expensive equipment, such as CT or X-ray imaging, which are limited in their resolution. To overcome these challenges, numerical simulations have emerged as an ideal method to study retrograde condensation and its flow dynamics. Compared with MD simulations, which require significant computational resources, numerical methods that use less computational power are preferred, for example, the lattice Boltzmann method.

A numerical method to successfully investigate the retrograde condensation of MC hydrocarbon fluids under a pressure drop in a porous media environment requires accurate prediction of the phase behavior of partially miscible MC fluids. Over the last three decades, the LB model has consistently shown potential for studying a wide variety of multiphase flow problems. In particular, the pseudo-potential (PP) LB models, also known as the Shan-Chen models, separate phases by incorporating proper external body forces. Pseudo-potential LB models have been widely applied to simulate fluid dynamics in various fields, including porous media, microfluidics, and multiphase flows. One notable advantage of PP LB models is their numerical simplicity and computational efficiency, which makes them an attractive option for simulating complex fluid systems. Simulations of multiphase mixture fluid flows have been previously conducted for various applications. Kamali & Van den Akker simulated dispersed gas-liquid fluid flows through an inclined microchannel with bends (14). Qin et al. conducted multiphase mixture simulations using the LB models, including the studies on evaporation and phase change in porous media (25), and geometric formulation scheme of modeling contact angle hysteresis in drying of porous media (26).

Zheng et al. characterized spontaneous imbibition dynamics in irregular channels (42). There are also relatively more fundamental studies on multiphase mixture flows using PP LB models. Li et al. modeled contact angles with curved boundaries (17). Wang et al. proposed two boundary-condition designs for MC fluids subject to pressure boundary conditions (35).

It is worth noting that most studies on multiphase flow in porous media are limited to immiscible fluids. In terms of partially miscible or miscible multiphase flows, to the best of the authors' knowledge, only two of the PP LB models can handle the thermodynamics of MC hydrocarbon fluid relatively correctly and have the capability to describe the phenomenon of retrograde condensation. These two models were proposed in previous studies (10, 21). The two models differ in their distribution of the external body force in each component. Although Gong and Cheng (10) designed a force distribution strategy through trial and error, Peng et al. (21) mathematically derived the force distribution based on the components' physical properties, such as volatility and composition, making it consistent with the definition of external body force in the PP LB models. While Peng et al.'s work focused on fluids under multiphase conditions, in this study, an improvement was made to Peng et al.'s model (21), which enables the simulation of partially miscible fluids under both single-phase and multiphase conditions.

Given previous attempts to model in situ natural gas condensation behaviors, only two studies have modeled partially miscible MCMP flows (5, 33). In one study (5), the condensate phase was uniformly introduced into the gas-filled pore space via a volumetric exchange process. To achieve equilibrium at a new phase saturation level, researchers introduced the condensate mass by source terms in each volume voxel while simultaneously and equally eliminating the gas phase through sink terms, using volumetric exchange as a method. However, this approach is not physically accurate because it does not rigorously consider the phase equilibrium of the gas condensate, and all properties should be predicted using an equation of state (EOS). In another study (33), the PP LB model was used to study the behavior of a single-component fluid. The model considered the pressure gradient and wetting-structure surfaces, causing condensates to drop out on the structure surface. However, this model is not suitable for studying the retrograde condensation of natural gas, as both natural gas and gas condensates are multicomponent mixtures. Additionally, the EOS adopted in this study was not sufficiently rigorous. The EOS used was a simplified version that did not correctly predict the thermodynamic behavior of a real fluid. To overcome this limitation, a more accurate EOS, such as the Peng-Robinson-EOS (PR-EOS), can be used (22, 23).

This paper presents a framework for investigating the retrograde condensation of partially miscible MCMP fluids in porous media. This framework integrates multiple state-of-the-art LB models, including an improved force-split model for single-phase/multiphase conditions, a fluid-structure model for achieving the desired wettability conditions, and a methodology for generating stochastic porous media (38). The desired wettability of the structural surface was achieved using a recently proposed model (20). This framework studies a binary component fluid consisting of methane (C_1H_4) and n-butane (nC_4H_{10}), or propane (C_3H_8) and n-pentane (nC_5H_{12}). The PR-EOS for fluid mixtures was used to represent the PVT relationships. The framework was applied to study the single-phase and multiphase behaviors and flow dynamics of such fluids in stochastic porous media under varying wettability conditions. Overall, the proposed framework can improve the understanding of the behavior of these fluids under different conditions, providing valuable insights into the qualitative evaluation of pore-scale multiphase flow mechanisms.

2. THE INTEGRATED FRAMEWORK

2.1. An improved MCMP PP LB model for partially miscible hydrocarbon fluids

This study utilizes the LB model with a multi-relaxation time (MRT) collision operator, which is widely recognized for its superior numerical stability and flexibility compared to other collision operators (15). In this study, a D2Q9 model (24) was applied to a multicomponent system, where the ith component had distribution functions. By using the MRT transformation, the distribution vector $\boldsymbol{f}_i$ is converted into its corresponding moments $\boldsymbol{m}_i$, such that $\boldsymbol{m}_i = \boldsymbol{M}\boldsymbol{f}_i$. The resulting LB equation is as **Equation 1**:

$$\boldsymbol{f}_i(\boldsymbol{x}+\boldsymbol{e}_\alpha\delta t, t+\delta t) - \boldsymbol{f}_i(\boldsymbol{x},t) \\ = -\boldsymbol{M}^{-1}\boldsymbol{S}\left[\boldsymbol{m}_i(\boldsymbol{x},t) - \boldsymbol{m}_i^{(eq)}(\boldsymbol{x},t)\right] + \boldsymbol{M}^{-1}\left(\mathbf{I} - \frac{\mathbf{S}}{2}\right)\boldsymbol{\Psi}_i(\boldsymbol{x},t)\delta t \tag{1}$$

On the right-hand side of this equation, the collision operator including external forces is represented, with the transformation matrix denoted as $\boldsymbol{M}$, and its inverse matrix as $\boldsymbol{M}^{-1}$ (16). Here, $\boldsymbol{e}_\alpha$ refers to the discrete velocity along the αth direction, while $\boldsymbol{x}$ and t denote the spatial and time coordinates, respectively. Each time step is denoted by δt, where $\boldsymbol{x}+\boldsymbol{e}_\alpha\delta t$ represents the locations of adjacent nodes. In the context of lattice Boltzmann methods with a D2Q9 discrete velocity set, the diagonal matrix $\boldsymbol{S}$ represents the relaxation parameters and is given by **Equation 2**:

$$\boldsymbol{S} = diag\left[\tau_\rho^{-1}, \tau_{\boldsymbol{e}}^{-1}, \tau_\varepsilon^{-1}, \tau_{\boldsymbol{j}}^{-1}, \tau_{\boldsymbol{q}}^{-1}, \tau_{\boldsymbol{j}}^{-1}, \tau_{\boldsymbol{q}}^{-1}, \tau_\nu^{-1}, \tau_\nu^{-1}\right] \tag{2}$$

The identity matrix is denoted by $\boldsymbol{I}$. The moments vector for the ith component is denoted by $\boldsymbol{m}_i$, and its equilibrium form is denoted by $\boldsymbol{m}_i^{(eq)}$. The forcing term in moment form for the ith component, denoted by $\boldsymbol{\Psi}_i$, represents external forces acting on the system.

An important concept in the MCMP fluid is the cell-volume density, denoted as $\bar{\rho}_i$ for the ith component. It refers to the mass of the ith component contained in the control volume of a lattice grid cell. $\bar{\rho}_i$ does not have a thermodynamic meaning in an MC system of miscible components. A thermodynamically meaningful density must be the mass of a substance per unit volume occupied by that specific substance. However, in an MC system with miscible components, the volume occupied by a specific component cannot be determined. For an MC system of miscible components, the only thermodynamically meaningful density, herein referred to as the thermodynamic density, is the density of the entire phase. In this work, $\bar{\rho}$ with an overbar is used to represent the cell-volume density of individual components, and ρ without an overbar represents the thermodynamic density of phases. Note that the density in any equation of state (EOS) must be the density of a phase rather than the cell-volume density of any individual component. We note this here because in many previous MCMP PP LB models, EOS was misused by inputting the cell-volume densities (1, 4, 8, 14, 34). More details regarding this observation can be found in our recent study (21). A more detailed elaboration of the EOS for this fluid of interest can be found in **Appendix A** (available online).

Macroscopic quantities are related to the distribution functions, as shown (**Eq. 3**):

$$\bar{\rho}_i = \sum_\alpha f_{\alpha,i} \qquad \rho = \sum_i \bar{\rho}_i \\ \rho\boldsymbol{u} = \sum_i\sum_\alpha f_{\alpha,i}\boldsymbol{e}_\alpha + \frac{1}{2}\sum_i \boldsymbol{F}_i\delta t \qquad \boldsymbol{F} = \sum_i \boldsymbol{F}_i \tag{3}$$

Using the Chapman-Enskog multiscale expansion (3), the continuity equation and the Navier-Stokes equation (NSE) in the incompressible limit can be reproduced by LBE, i.e. **Equation 4a** & **b**, where $\mathbf{I}$ is a unit matrix and $\mathbf{T}$ is the viscous stress tensor.

$$\frac{\partial\rho}{\partial t} + \nabla\cdot(\rho\mathbf{u}) = 0 \tag{4a}$$

$$\frac{\partial\rho}{\partial t}(\rho\mathbf{u}) + \nabla\cdot(\rho\mathbf{u}\mathbf{u}) = \nabla\cdot(-c_s^2\rho\mathbf{I} + \mathbf{T}) + \mathbf{F} \tag{4b}$$

Note that, similar to EOS, a physically meaningful NSE must be applied to the entire phase rather than to individual components.

Pseudo-potential LB models simulate multiphase behaviors by incorporating external body forces $\mathbf{F}$ (which are usually referred to as Shan-Chen forces) as the macroscopic representation of the molecular interactions between the local fluid and its neighbors (12, 28, 30). In classic MCMP PP LB models applied to immiscible components, usually the external body force for every component, i.e., $\mathbf{F}_i$ is defined directly (12, 30). However, for a partially miscible MC fluid, since all the components form a homogeneous mixture within each phase, it is only thermodynamically meaningful to define the total Shan-Chen force in terms of the phase combining all components. The definition of this total Shan-Chen force is analogous to its definition in the single-component multiphase (SCMP) PP LB models (28, 29) (**Eq. 5**), where G is the intensity of the force and w_α is the weighting factor that can simply use its counterpart in the equilibrium distribution functions of the lattice Boltzmann equation (LBE).

$$\mathbf{F}(\boldsymbol{x}) = -G\psi(\boldsymbol{x}) \sum_{\alpha} w_\alpha \psi(\boldsymbol{x} + \boldsymbol{e}_\alpha)\, \boldsymbol{e}_\alpha \tag{5}$$

To incorporate thermodynamic information into the MCMP PP LB model, effective mass ψ is defined in terms of the density of the phase by using an EOS applied to MC mixtures (**Eq. 6**), where $p_{EOS}\,(\rho)$ is the thermodynamic pressure computed from the chosen EOS with the density of phases. When ψ is defined with **Equation 6**, the intensity of Shan-Chen force G no longer controls the magnitude of the external body force and instead only ensures that the whole term under the square root is non-negative.

$$\psi = \sqrt{\frac{2(p_{EOS}(\rho) - c_s^2 \rho)}{G c_s^2 \delta t}} \tag{6}$$

The Shan-Chen force defined in **Equation 5** is the total force acting on the phase, including all its components. As stated before, there are two main physical considerations in the design of the force split coefficient: first, the force must be proportional to the cell-volume density and composition of one component, and second, the less volatile components are likely to have a greater share in the total force. Following these two considerations, under multiphase conditions, the force-split scheme proposed in (21) (original force split model) is used, such that (**Eq. 7**):

$$\boldsymbol{F}_1(\boldsymbol{x}) = \kappa_1 \boldsymbol{F}(\boldsymbol{x}) \qquad \boldsymbol{F}_2(\boldsymbol{x}) = \kappa_2 \boldsymbol{F}(\boldsymbol{x}) \qquad \boldsymbol{F}_3(\boldsymbol{x}) = \kappa_3 \boldsymbol{F}(\boldsymbol{x}) \; \ldots \tag{7}$$

$$\sum_i \kappa_i = 1 \qquad \kappa_i = \frac{\gamma_i \bar{\rho}_i V}{\sum_i \gamma_i \bar{\rho}_i V}$$

where κ_i and γ_i are the force split coefficient and force split factor of the ith component respectively. γ_i depends on the pressure and temperature of the system.

Consider a binary system - the original assumption of constant values of γ_i for the entire simulation domain is inconsistent with the varying pressure and volatility values for different phase conditions. A simple and practical solution would be to assign γ as a piecewise function that varies depending on whether the system is under single-phase or multiphase conditions (piecewise force split model).

In our investigation of multiphase conditions, for a binary mixture system (components 1 and 2) to be consistent with how the Shan-Chen force was defined as Peng et al.'s original force split scheme, γ_i must be given by the following formulations. Assume that component 1 is the less volatile component (generally heavier component) (**Eq. 8** & **Eq. 9**), where $\bar{\rho}_{i,L}$, and $\bar{\rho}_{i,v}$ are the cell-volume densities for the ith component (defined as in **Eq. 9**) in the liquid and the vapor phases, respectively.

$$\gamma_i = \frac{ln(\bar{\rho}_{1,l}/\bar{\rho}_{1,v})}{ln(\bar{\rho}_{2,l}/\bar{\rho}_{2,v})} = \frac{ln(\tilde{\rho}_l/\tilde{\rho}_v) - lnK_1}{ln(\tilde{\rho}_l/\tilde{\rho}_v) - lnK_2} \qquad \gamma_2 = 1 \tag{8}$$

$$\bar{\rho}_1 = \rho \frac{c_1 M_1}{c_1 M_1 + c_2 M_2} \qquad \bar{\rho}_2 = \rho \frac{c_2 M_2}{c_1 M_1 + c_2 M_2} \tag{9}$$

M_i is the molar mass of the ith component. $K_i = y_i/x_i$ is the equilibrium ratio of the ith component, which is the ratio between the molar fraction in the vapor phase, y_i, and the molar fraction in the liquid phase, x_i.

The originally proposed scheme has a limitation in the single-phase region. As retrograde condensation is the fluid behavior of interest, the initial pressure condition should be above the upper dew point pressure so that the fluid is in a single-phase condition. If we follow **Equation 8**, we will find that K_i cannot be calculated when the number of phases is only one because K_i is a physical property defined only under multiphase conditions. Therefore, the single-phase scenario needs to be re-derived instead of using Peng et al.'s universal γ, which is only applicable to multiphase conditions. Details on the derivation can be found in **Appendix B** (available online).

Under single-phase conditions, we found that the only way to ensure that a single-phase fluid remains in only one phase is when γ_1 and γ_2, are both equal to 1. A generic discontinuous piecewise definition of γ_i can be obtained by grouping the single-phase and multiphase expressions. During simulations, the value of γ_1 varies depending on the grid point's phase condition, which is determined by whether the local grid pressure falls within the multiphase pressure region specified on a phase envelope. For example, in **Figure 1**, if local pressure is within the multiphase range (~220 psi to ~1870 psi), then we have **Equation 10**, otherwise $\gamma_1 = 1$ (**Eq. 11**).

$$\gamma_1 = [ln(\tilde{\rho}_l/\tilde{\rho}_v) - lnK_1]/[ln(\tilde{\rho}_l/\tilde{\rho}_v) - lnK_2] \tag{10}$$

$$\gamma_2 = 1 \qquad \gamma_1 = \begin{cases} 1 & single\ phase \\ \dfrac{ln(\tilde{\rho}_l/\tilde{\rho}_v) - lnK_1}{ln(\tilde{\rho}_l/\tilde{\rho}_v) - lnK_2} & multiphase \end{cases} \tag{11}$$

For a specific component in a grid cell, the force it experiences should be proportional to its mass composition. When $\gamma_1 = \gamma_2 = 1$, a uniform composition can be maintained, and no more than one phase occurs. The composition is initialized to be uniform, and the ratio of forces shared by each component remains constant. However, for multiphase conditions where $\gamma_1 < \gamma_2 = 1$, the split coefficient $\kappa_{1,mp}$ (**Eq. 7**) is greater than $\kappa_{1,sp}$ (**Eq. B4** in **Appendix B**, available online), where the subscripts mp and sp represent multiphase and single-phase conditions, respectively. This is because a larger portion of the Shan-Chen force is distributed to the less volatile, and generally heavier, component 1. In multiphase

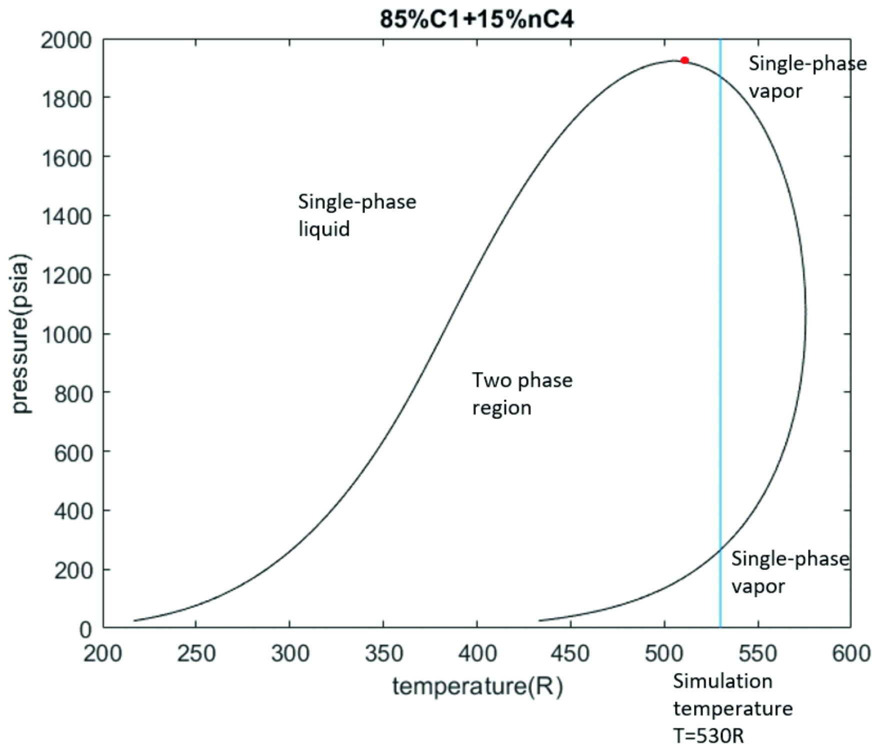

Figure 1: Phase envelope of 85%C1+15%nC4. The blue line represents the simulation temperature at 530R°. The red dot marks the critical point.

conditions, the Shan-Chen force generally points toward higher-density regions. As a result, component 1 tends to move toward higher-density regions compared to component 2. Over time, this regional variation in density becomes more pronounced, and eventually, it leads to more than one phase occurring. The split coefficient κ_1 becomes even greater at higher-density regions, as the local composition of the heavier component 1 increases, while the opposite occurs in lower-density regions. This phenomenon allows for the realization of multiphase environments in the domain.

2.2. Fluid-structure interactions schemes

Properly handling fluid-structure interactions is indispensable for simulating multiphase flows in porous media structures. The structural surfaces of porous media are required not only to enforce the impenetrable, no-slip condition but also to generate physical contact angles for the interacting liquid phase. In this framework of PP LB models, specific contact angles are achieved by designing analog Shan-Chen forces on the boundary nodes contributed by the neighboring nodes within the structure region (2, 6, 11, 18).

Previous studies have developed fluid-structure interaction forces for pure substances in the context of fluid–structure interactions using mesoscopic simulations. One such force was developed by Benzi et al., and involves a constant virtual fluid density in the structure (2). However, this approach has been shown to generate a nonphysical mass-transfer layer between the droplets and structure. To overcome this issue, Li et al. developed an improved fluid-structure interaction scheme that uses a localized virtual fluid density defined as a function of the local averaged fluid density to eliminate the nonphysical mass transfer layer (17). This localized virtual fluid density was adjusted to achieve a target contact angle, and was confined between the saturated vapor and liquid densities using a limiter. The confined value of the effective mass of the structure sometimes introduces artificial influences, particularly when curved interfaces and associated capillary pressures exist (20).

Though Li et al.'s (17) The fluid-structure interaction scheme significantly mitigates the issue of the "unphysical mass transfer layer"; it is not a perfect scheme for this partially miscible fluid because of its lack of simplicity. For MCMP, PP ψ depends on both local cell-volume densities and the molar fraction. Under this multi-independent variable condition, it is difficult to simultaneously tune ρ_w and $c_{w,i}$ to achieve the desired wetting condition.

In their recent work, Peng et al. (20) proposed a novel approach to control the wetting conditions in fluid-structure interactions by defining the appropriate pressure potential (ψ_w) at structural locations. This approach is considered to be a more natural way to define virtual density at structural locations while also considering the molar compositions of adjacent components. Similar to Li et al., who defined fluid–structure interactions using local information (17), Peng et al. (20) propose a fluid-structure interactions scheme (**Eq. 12**),

$$\boldsymbol{F}_w(\boldsymbol{x}) = G\psi(\boldsymbol{x})\sum_{\alpha} w_\alpha \psi_w(\boldsymbol{x}+\boldsymbol{e}_\alpha\delta t)s(\boldsymbol{x}+\boldsymbol{e}_\alpha\delta t)\boldsymbol{e}_\alpha \tag{12}$$

Shown in **Equation 13** and **14**:

$$\psi_w(\boldsymbol{x}) = \phi_w\psi_{ave}(\boldsymbol{x}) \tag{13}$$

$$\psi_{ave}(\boldsymbol{x}) = \frac{\sum_\alpha w_\alpha s'(\boldsymbol{x}+\boldsymbol{e}_\alpha\delta t)\psi(\boldsymbol{x}+\boldsymbol{e}_\alpha\delta t)}{\sum_\alpha w_\alpha s'(\boldsymbol{x}+\boldsymbol{e}_\alpha\delta t)} \tag{14}$$

with ϕ_w to control the resulting contact angle: when $\phi_w > 1$, contact angle $\theta < 90°$, while when $\phi_w < 1$, $\theta > 90°$. The values for s and s' are solid phase and fluid phase indicators of either 0 or 1.

In this study, the fluid–structure interaction scheme proposed by Peng et al. was selected over the previous two schemes for several reasons. First, their approach directly constructs the pressure potential (ψ_w) instead of indirectly computing it through a virtual density (ρ_w), resulting in only one parameter (ϕ_w) required to control wettability, which is more straightforward and convenient. Second, Peng et al. used a uniform scheme for contact angles ranging from 0° to 180°, eliminating the need for a piecewise function, as shown in Li et al.'s scheme (17). Third, they did not add a limiter to confine the pressure potential (ψ_w). Finally, their approach did not result in the creation of an unphysical mass-transfer layer. By using this selected model, it becomes possible to simulate the phase behavior of the MCMP hydrocarbon mixture in porous media under different wettability conditions.

2.3. Porous medium structures

In this study, porous medium structures were generated using two-dimensional (2D) Voronoi tesselation (VT). There are two main reasons for choosing a VT porous medium over realistic pore geometries: better connectivity and avoiding the need to resolve flows in small throats. In **Figure 2**, porous medium structures with and without periodicity from the 2D VT are illustrated.

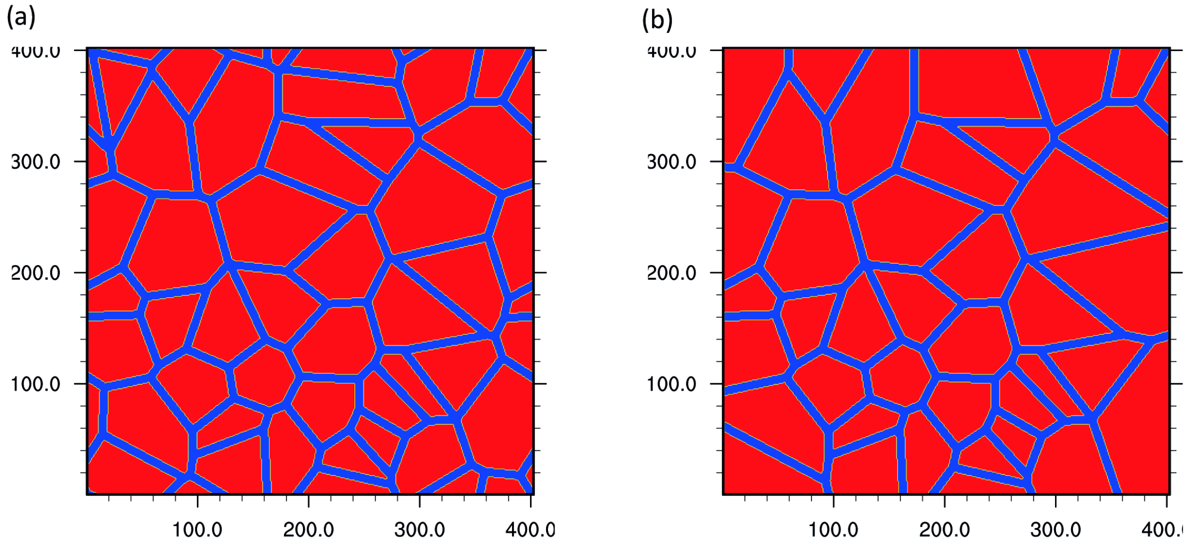

Figure 2: 2D porous medium structures generated with 2D VT (40 Poisson seeds) in a 400 × 400 domain with channel width $\boldsymbol{W = 8\delta x}$: **(a)** with periodicity, porosity 23.84%; **(b)** without periodicity, porosity 20.57%.

The generation process consists of three steps. First, random Poisson seeds are distributed in a 2D domain. When periodicity is required in both directions, the locations of these random Poisson points are copied to the eight neighboring domains. Subsequently, a standard VT was used to generate edges based on the distributed Poisson seeds. Finally, the edges were expanded to the desired width to create channels as the pore phase in the porous medium structures. Additional details can be found in the work by Xiao (38).

A sufficient grid resolution is required to represent the channel width such that the flow properties of interest can be accurately obtained. To fully resolve the flow in a specific inclined channel, a fine grid resolution of $W \geq 40\delta x$ is needed to reduce the error of the mass flux in the channel to less than 1% (δx here denotes the LB spatial unit). This, however, is too costly. Instead, to resolve flow in each pore, for flows in porous media, it is usually the bulk permeability being used (**Eq. 15**), where v is the fluid flow velocity in the porous media, μ is the dynamic viscosity, L is the characteristic length of the porous media, and Δp is the applied pressure difference at two different porous media ends. The requirement for grid resolution can be significantly relaxed owing to the cancellation of numerical errors from the individual channels.

$$k = \frac{\mu v L}{\Delta p} \tag{15}$$

To obtain grid resolution results with sufficiently accurate permeability, a grid convergence study was conducted on the periodic porous medium structure shown in **Figure 2**. The periodicity was chosen only to take advantage of its simpler boundary treatment by applying periodic boundary conditions. Selection should not affect the generalizability of observations. The convergence study was conducted with a single-phase flow driven by uniform body force $\rho g = \Delta P/L$, where L is the length of the domain in both directions. In **Figure 3** , we show the relative errors of the porosity, computed as n_{fluid}/n_{total}, where n_{fluid} and n_{total} are the number of grid points in the pore phase and the total number of grid points, respectively. k/L^2 is the normalized permeability in each direction for different grid resolutions. The benchmark results are from the simulation with the highest grid resolution of $W = 24\delta x$ in a 1200 × 1200 domain. To eliminate the possible Reynolds number ($Re = \rho vL/\mu$) dependency, the errors of permeability over six flows, ranging from 0.016 to 0.9, were averaged.

As shown in **Figure 3**, the permeability errors in both directions were less than 3%, with a grid resolution of $W = 8\delta x$. This is similar to the observation by Xiao that a channel width of $6\delta x$ can maintain a relative error of permeability of approximately 3% in the Darcy/Stokes flow limit (38). It should be noted that the aforementioned convergence study was conducted using a single-phase fluid. As it is difficult to extend this convergence study to a multiphase flow, we simply doubled the grid resolution requirement for multiphase flow applications, i.e. a grid resolution $W \geq 16\delta x$ was considered sufficient to retain accurate permeability for each phase in the idealized porous medium structures generated by the VT.

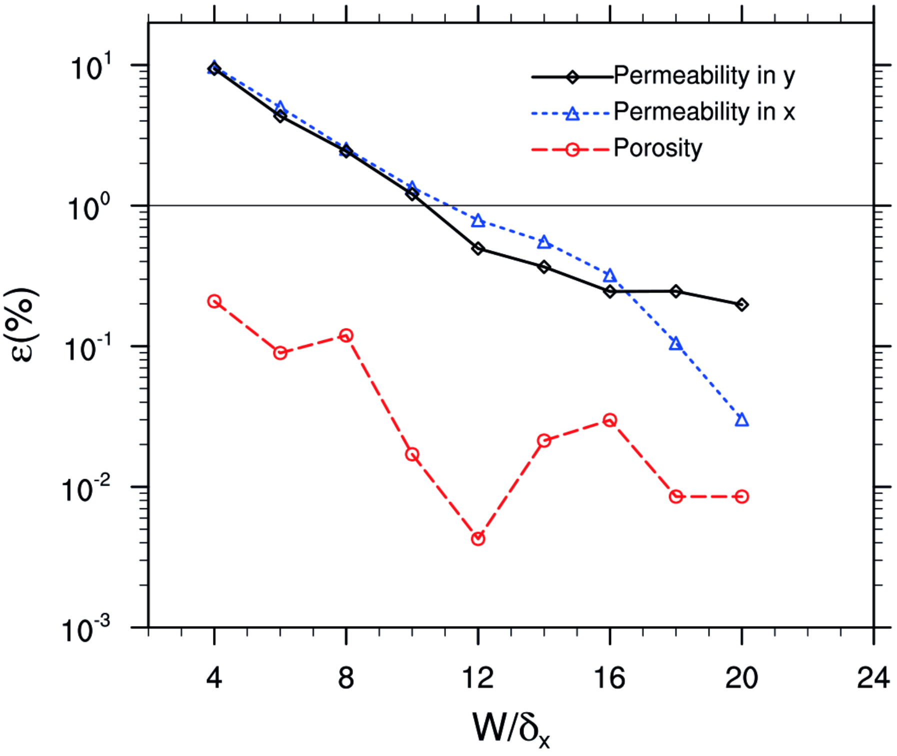

Figure 3: Relative errors of porosity and permeability with different channel widths for the porous medium structure in **Figure 2a,** benchmarked with the highest grid resolution of $W = 24\delta x$ in a 1200 × 1200 domain from Xiao's work (38).

There are two criteria for determining a sufficient channel width. First, a sufficient channel width covers enough grid points to resolve the flow, or at least accurately captures the total mass flux across its cross-section. Second, the volume occupied by the two-phase interface must only be a small portion of the total pore area because the thickness of the two-phase interface is very thin. To ensure that this fact is well represented in the simulation, the ratio between the interface thickness D and the channel width W should be a small number. We suggest that this ratio not exceed 0.2, such that in a 2D simulation, the interfaces do not occupy more than 5% of the total volume.

2.4. Scaling system

The scaling system in LB simulations plays a pivotal role in guaranteeing that simulation results are physically meaningful. Currently, LB simulations lack a physically reasonable scaling system for real hydrocarbon (HC) fluid mixtures. This oversight has not been fully recognized in previous studies. Recent studies by Zhao et al. have reported length scales at molecular sizes (0.35 nm-0.4 nm) (40, 41). This may pose a problem, as the LB models' statistical presumption is that one lattice should encompass at least hundreds or thousands of molecules. Such a packing level may even fall below the co-volume of the EOS. Considering the continuum of HC molecules, pore throat sizes, and various materials, it is crucial to ensure a sufficient pore volume space for the total volume of molecules assumed in the simulations. A minimum requirement is that the pore volumes in the LB simulations should be significantly higher than the volume at maximum compaction. Pore volumes at the scale of 10^{-1} nm lack physical meaning, and a pore volume must be of 10^{1} nm or greater for LB simulations to be physically meaningful. Wang detailed a tunable surface-tension scheme to obtain a scaling system for HC fluid mixtures in a recent study (38). To systematically obtain the scaling system of MCMP at the pore scale when working with HC binary mixtures, the lighter component of the two is typically chosen for scaling purposes. Consider, for instance, an HC fluid composed of 85% C1 and 15% nC4. Please see **Table 1** for the physical properties of C1 and nC4.

Table 1: Physical properties of C1 and nC4.

	p_c (psi)	T_c (°R)	$MW\ (lbm/lbmol)$	ω
C1	666.4	343.33	16.043	0.0104
nC4	550.6	765.62	58.123	0.1995

In such a case, ω in **Table 1** means Pitzer's acentric factor (23), and the critical point of C1 is utilized for scaling purposes. The reasoning is as follows: first, the lighter component gives smaller length and time scales; second, it is difficult to obtain the local composition at a certain time frame because simulation is a dynamic process. In addition, existing LB model scales rarely consider the restraints of scales introduced by thermodynamics (the EOS). In single-component systems (38) or immiscible multiphase fluids, when significant changes are not observed in the PVT behavior, the resolution is ultimately governed by the capabilities of the CT scanner. However, for partially miscible MCMP fluids, the scaling system depends on various units, including the three EOS parameters of a, b, and R, interfacial tension σ, and the molecular weight MW. Either σ or fluid viscosity ν can be used to obtain the time scale (15). However, when a flow with multiphase phenomena exists, the σ scaling path is the proper one to follow. Another reason for avoiding the ν scaling path is that simulation stability is sensitive to the ν value. In this study, where the primary interest lies in investigating phase behaviors, σ was therefore selected. If χ represents the scale, then the scaling system is given as **Equation 16** where L, t, M, N , and T represent five basic independent units' length, time, mass, amount of substance, and temperature respectively. The derivation is detailed in **Appendix C** (available online).

$$\chi_L = (\chi_\sigma)(\chi_b)^2(\chi_a)^{-1} \tag{16}$$

$$\chi_t = (\chi_{MW})^{\frac{1}{2}}(\chi_\sigma)(\chi_b)^{\frac{5}{2}}(\chi_a)^{-\frac{3}{2}}$$

$$\chi_M = (\chi_{MW})(\chi_\sigma)^3(\chi_b)^5(\chi_a)^{-3}$$

$$\chi_N = (\chi_\sigma)^3(\chi_b)^5(\chi_a)^{-3}$$

$$\chi_T = (\chi_R)^{-1}(\chi_b)^{-1}(\chi_a)$$

3. NUMERICAL STUDIES

In this section, the integrated method is used to demonstrate its ability to generate multiphase behaviors, and model validation is conducted to examine its capacity to simulate various wettability conditions. In the simulation case, the phase changes of the fluid under lower-pressure outflow boundary conditions were investigated in the VT porous media. Although previous studies have examined the flow of SCSP fluids in VT porous media (38), this study is the first to simulate partially miscible MCMP fluids in such porous media. Additionally, different wettability conditions were tested to examine their influence on the MCMP flow phase behavior.

3.1. Model validation

The first case study to validate the integrated framework was to simulate a static droplet attached to a wall. The primary objective of this validation was to demonstrate the capability of the integrated framework to predict the wetting behavior of a droplet on a flat structure surface under different thermodynamic conditions, which is a simplified version of the following study case in porous media. In comparison to a previous work (20), which utilized the original force split model (21) to simulate partially miscible fluids, the present study utilized the improved MCMP PP LB model introduced before to simulate partially miscible multiphase fluids.

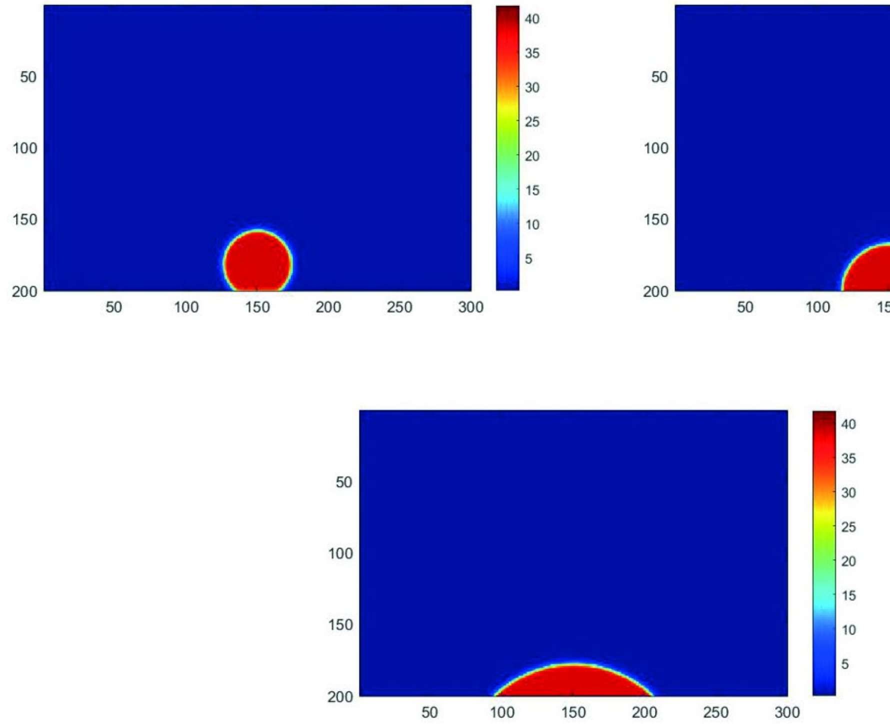

Figure 4: Static contact angle of the binary system of $\boldsymbol{C_3 + nC_5}$. From top to bottom (left to right), the values of $\boldsymbol{\phi_w}$ are inputted as 0.8, 1.0, and 1.2, and contact angles $\boldsymbol{\theta}$ are measured as approximately 120°, 90°, and 60°, respectively.

The case of a static droplet contacting a flat structure wall was adopted with domain size $N_x \times N_y = 300 \times 200$. The thermodynamic properties of the binary systems of C_3 and nC_5 are simulated at the thermodynamic equilibrium, and the PVT conditions are temperature set to be 550°R, pressure 40 *psi*, the molar fraction of C_3 in the liquid phase $x_1 = 0.202$, and the molar fraction of C_3 in the vapor phase $y_1 = 0.723$. The mass density of the liquid phase is $\rho_{\iota,sat} = 38.441 lbm/ft^3$, and the mass density of the vapor phase is $\rho_{\iota,sat} = 0.374 lbm/ft^3$, which makes the ratio of the density of vapor phase and liquid phase approximately 100 (lbm here denotes Pounds-mass). The initial cell-volume density field for the ith component is defined as **Equation 17**, where $\bar{\rho}_{i,l,sat}$ and $\bar{\rho}_{i,v,sat}$ are computed based on the material balance as **Equation 18**.

$$\bar{\rho}_i(x, y, t = 0) = \frac{\bar{\rho}_{i,l,sat} + \bar{\rho}_{i,v,sat}}{2} + \frac{\bar{\rho}_{i,l,sat} - \bar{\rho}_{i,v,sat}}{2} tanh\left[\frac{2\left(\sqrt{(x - x_c)^2 + (y - y_c)^2} - R_0\right)}{W}\right] \tag{17}$$

$$\bar{\rho}_{i,l,sat} = \rho_{l,sat}\frac{x_i M_i}{\sum_i x_i M_i} \qquad \bar{\rho}_{i,v,sat} = \rho_{v,sat}\frac{y_i M_i}{\sum_i y_i M_i} \tag{18}$$

Based on the simulation results shown in **Figure 4**, the three conditions of $\phi_w = 0.8, 1.0, and\ 1.2$ are simulated (from top to bottom). The corresponding contact angles measure approximately 120°, 90°, and 60°, respectively. As reported by the authors, the value of $\phi_w - 1$ can be conveniently related to the value of $\cos(\theta)$ as a linear equation (m is the slope), such that (20) (**Eq. 19**):

$$\cos(\theta) = m(\phi_w - 1) \tag{19}$$

A similar relationship is observed in the present study. **Figure 5** shows a comparison between the contact angles obtained from another study (20), the present results, and the prediction using **Equation 19**. The slope of the straight line depends on the selection of fluid and temperature. The present work matches well with the linear prediction results, indicating that the selected wettability model within the integrated framework can predict the wetting behavior of multiphase fluids under different thermodynamic conditions. Furthermore, the desired wettability condition (contact angles) can be conveniently and accurately acquired by adjusting the parameter ϕ_w.

3.2. Porous medium

A partially miscible binary component fluid consisting of 85% C1 plus 15%nC4 flow in a VT porous medium is simulated with the proposed framework. The channel width D is selected as $16\delta x$ to retain sufficient resolution for each phase, as illustrated in **Figure 6**. Twenty Poisson seeds were used in the VT; using too many seeds may lead to large porosity. Such a porous medium is generated without periodicity because different boundary conditions are applied to different boundaries. The porosity was measured to be 23.6%.

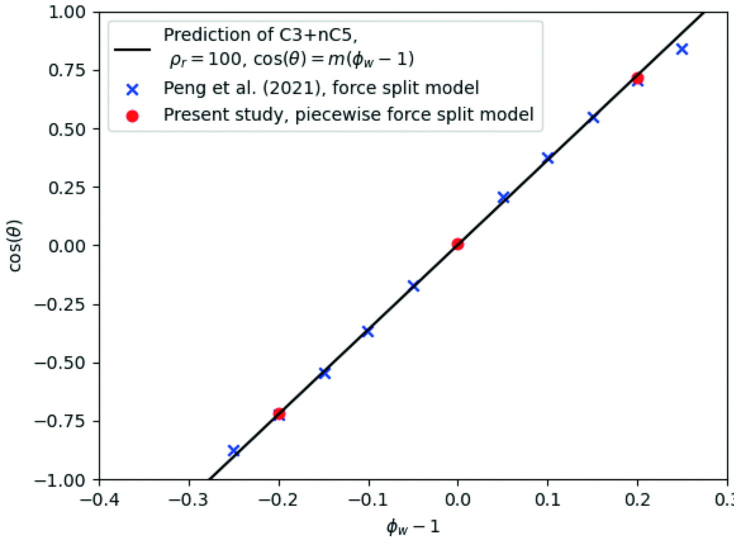

Figure 5: The comparison between the actual contact angles from Peng et al.'s (22) results, the present results, and the prediction by **Equation 19**.

The absolute permeability of this VT porous medium was measured using 100% C1 fluid. The temperature was set at T = 530 Rankine ($R°$) (= 21.1C°), and the inlet was the pressure condition while the outlet was the velocity condition, maintained at: $v_{out} = 5e - 5\ \delta x/\delta t$ before and after reaching stabilization. The averaged pressure difference between the two ends was measured as $\Delta p = 0.031$. According to Darcy's law, the absolute permeability for this porous medium was measured as 3.904 in LB units or 0.0153 in dimensionless form ($k_D = k/D^2$). The other parameters are as follows: ν is the fluid kinematic viscosity set at 2.7 $\delta x^2/\delta t$ and 65 $\delta x^2/\delta t$, water density is $\rho = 2.2$, and L is the porous medium domain length, which equals $400\delta x$.

As shown before, with a grid resolution of $W = 16\delta x$, the error of permeability in each of the two directions is less than 1%. This is close to the observation made in Xiao's work (38) that a channel width of $6\delta x$ can maintain a relative error of permeability around 3% in the Darcy/Stokes flow limit. The measured $k_D = 0.0153$ is within the range of Xiao's permeability measurements, 10^{-3} to 10^{-2}.

3.3. Simulations in the porous medium

The VT domain in **Figure 6** with the resolution of $W = 16\delta x$ was used for the simulations, and the flow was driven by velocity boundaries. The modified Non-Equilibrium Bounce Back (mNEBB) scheme for MCMP in one study (35) was leveraged here for fixed velocity in this case. The material loss leads to pressure dropout, and therefore generates retrograde condensation behaviors. Both simulations are set at a constant temperature above the critical temperature, but below the cricondentherm, e.g., T = 530 Rankine (R°) (=21.1°C), as indicated by the solid blue vertical line in **Figure 1**. The fluid is a super-critical vapor when the physical initial pressure is slightly above the envelope at 1872 psi, 2 psi above $p_{dew} = 1870\ psi$. The total domain is set to $500\delta x$ (horizontal) by $400\delta x$ (vertical), including $100\delta x$ as the buffer zone. The top, right, and bottom boundaries are closed-wall boundaries, and the bounceback scheme is applied. The left boundaries are outlets. The horizontal velocity u_x is uniformly set to $0.002\ \delta x/\delta t$ to drive the flow, while the vertical velocity u_y is set to 0. The reason for setting up 100 layers of a buffer zone is to reduce the effects of zero-vertical velocity. Three wetting conditions are applied by setting the fluid-structure interaction parameter ϕ_w to the values of 1.00, 0.95, and 1.05 to achieve the neutral, gas-wet, and liquid-wet conditions, respectively. The contact angles are approximately 90°, 105°, and 75°, respectively. Please see **Table 2** for the simulation conditions in VT domains. The density maps under different wetting conditions are presented in **Figure 7**, and the pressure maps at a time interval of 25000 ts (time step, equivalent to δt) are presented **Figure 8**. The piecewise γ model is applied to generate the multiphase behaviors. Other parameters, e.g., a, b, and R in PR-EOS, are inputted as 0.1837, 0.1044 (39) and 1, all of which are in LB units. The value of b is optimized concerning the maximum condensate saturation, largest length scale, and simulation numerical stability. The viscosity ν is set to 0.1137, which leads to a Reynolds number $(Re = uL/\nu)$ and a Weber number $(We = \rho u^2 L/\sigma)$ equal to 7.04 and 3.62 respectively. The scale of LB spatial unit can be obtained via the scales of a, b, R, interfacial tension σ, and molecular weight MW, and it is taken as $0.01\mu m/\delta x$ via **Equation 16**. To obtain this scale, the universal gas constant is taken as R_{phy} = 10.73psi ft^3/lbmol °R = 49712.69 lbm/ft·s^2. Meanwhile, the physical σ values reported in previous studies (19, 31) were referred to here, at temperature T = 530°R, σ = 0.6mN/m = 0.00132lbm/s^{-2}.

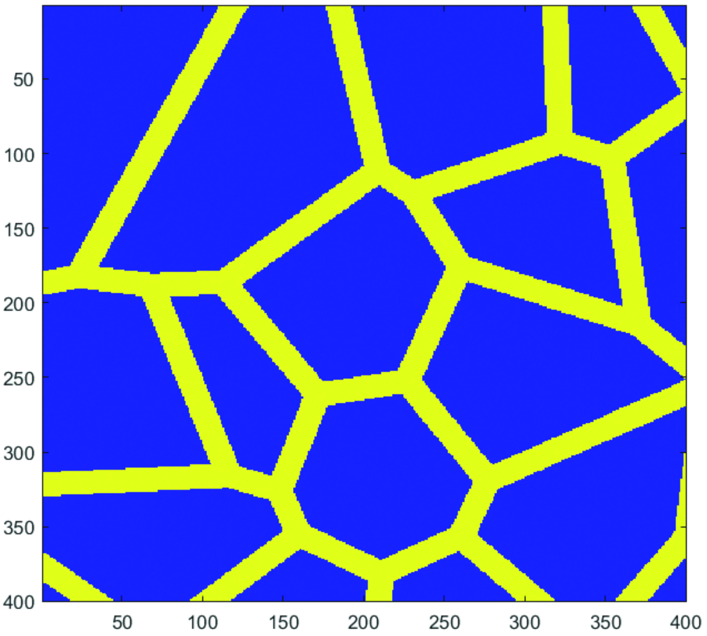

Figure 6: 2D porous medium structures generated with 2D VT (20 Poisson seeds) in a 400 × 400 domain with channel width $\boldsymbol{W = 16\delta x}$, porosity is measured as 23.6%. Yellow marks the pores (channels).

Table 2: Simulation conditions in VT domains.

Number	Fluids	ϕ_w	Contact Angle	Outlet BC	γ_1
1	85%C1 + 15% nC4	1	90°	Uniform, 0.002	0.081
2	85%C1 + 15% nC4	0.95	75°	Uniform, 0.002	0.081
3	85%C1 + 15% nC4	1.05	105°	Uniform, 0.002	0.081

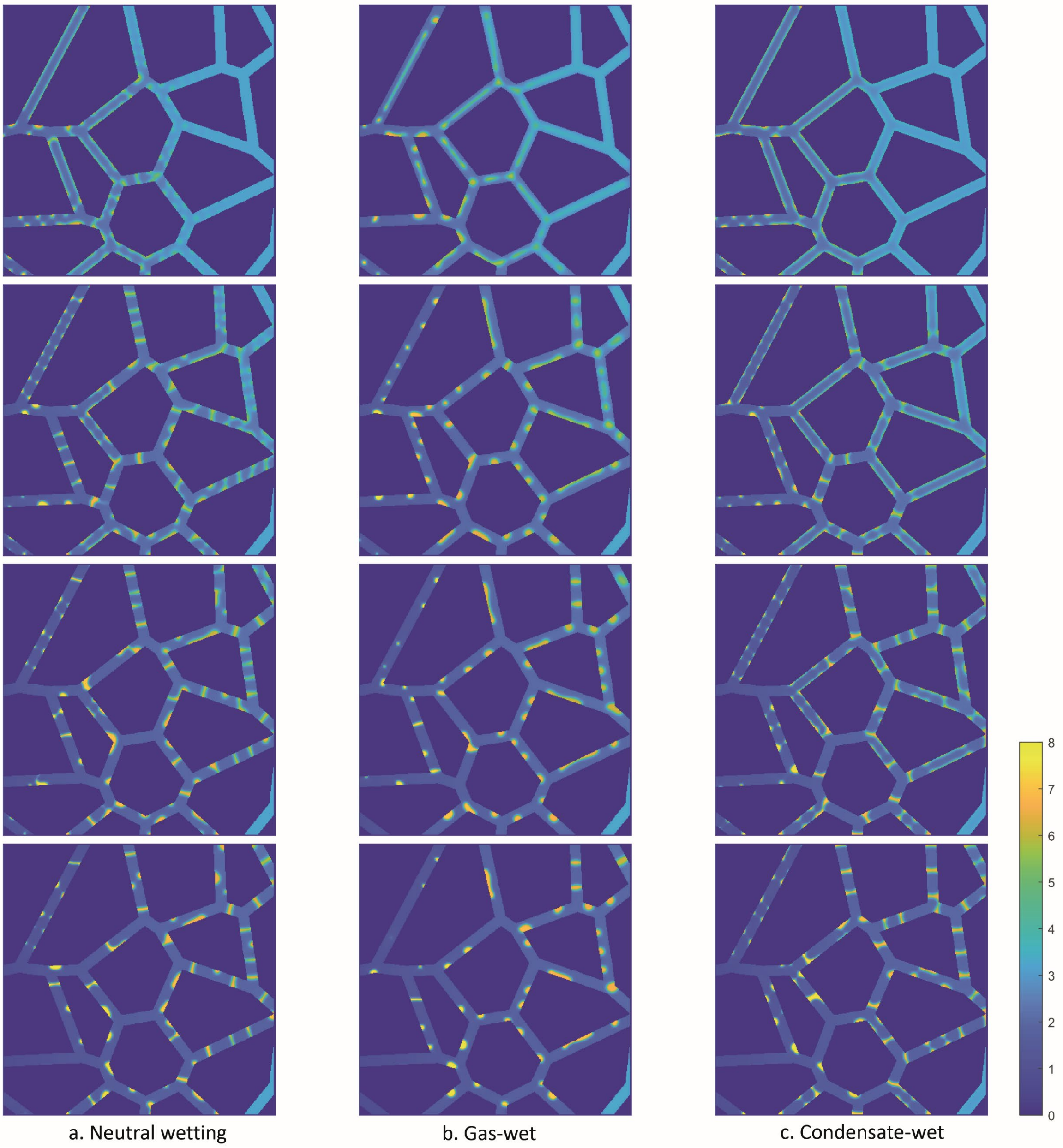

Figure 7: Evolution of density distribution of 85%C1+15%nC4 system of different wettability conditions. Light blue represents the gas phase, while yellow indicates the condensate oil phase, and both phases are flowing toward the outlet. Four time frames of 25000, 50000, 75000, and 100000 ts are shown, from top to bottom.

Both simulations stop at 100000 ts. Further simulation will lead to over-depletion near the outlet area and, in turn, an excessively large density ratio between the phases at the outlet section and those at the deep domain section. Further investigation is required to fully resolve the issue of a large density ratio.

Although not evident, pressure differences across phases resulting from capillarity effects can still be observed. When retrograde condensation starts, the light (C1) and heavy (nC4) components in the mixture exhibit dissimilar miscibility in the liquid and vapor phases. In contrast to Schembre-McCabe et al.'s condensate-dropout method (5), the present method uses thermodynamic models to rigorously predict the composition of components in both phases. The piecewise γ model can proportionaly split the Shan-Chen force into two components and enforce the components across the interfaces.

As shown in **Figure 7**, as time evolves, the yellow condensate phase drops out from the light blue gas phase and starts to form in the middle of the channel (**Figure 7b**), as the condensate phase is a non-wetting phase, or attached to the structure channel structures (**Figure 7a** & **c**). Meanwhile, the velocity boundary drives the fluid flow outside the domain (to the left) and simultaneously creates a pressure drop that allows more condensate to form. The droplets and film start to flow outside of the domain. Initially, they appear in the shape of globules and attach to the structure surface. As the domain pressure gradually decreases, the amount of condensate grows larger, and the density difference between the two phases becomes more distinct, due to the heavier component nC4 gradually transferring toward the liquid phase. A higher concentration of nC4 is also observed in the fluid phase area while a lower concentration is in the vapor phase area. The larger droplets begin to merge, forming larger irregularly shaped films and droplets or slugs. The VT process may result in isolated sections appearing in the bottom-right corner, specifically in the region where no condensation occurs. This difference indicates that pressure likely serves as the primary factor that triggers the phase changes.

The shapes of the condensate phases under different wetting conditions also exhibit distinct patterns. In the wetting phase, the liquid phase tends to reside at the surface, making it more difficult for fluids to flow out of the domain, resulting in the formation of rounded droplets or thicker films. When the

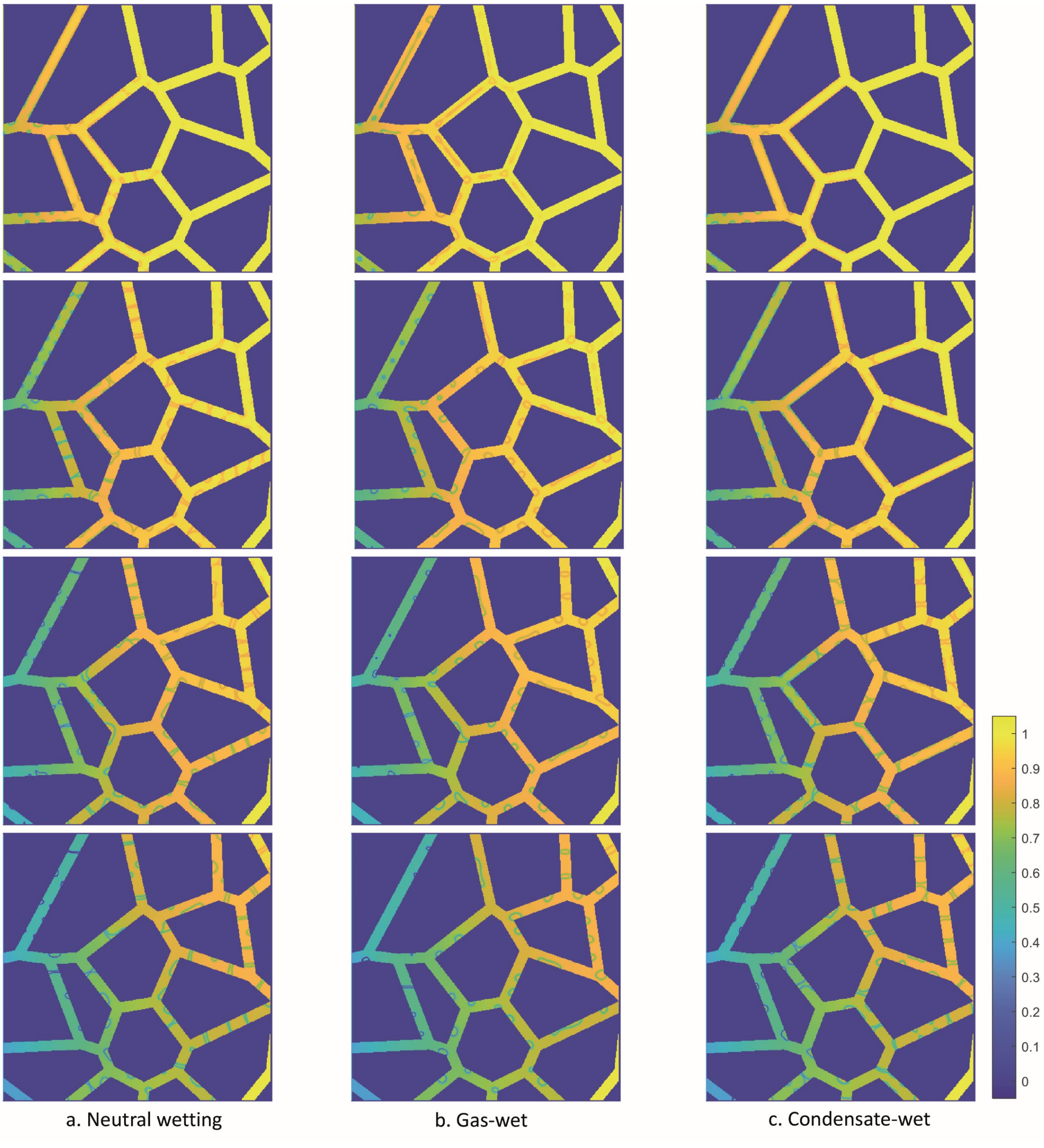

a. Neutral wetting b. Gas-wet c. Condensate-wet

Figure 8: Evolution of pressure distribution of 85%C1+15%nC4 system of different wettability conditions. Lighter colors represent higher pressure values. The interface can be observed clearly. Four time frames of 25000, 50000, 75000, and 100000 ts are shown, from top to bottom.

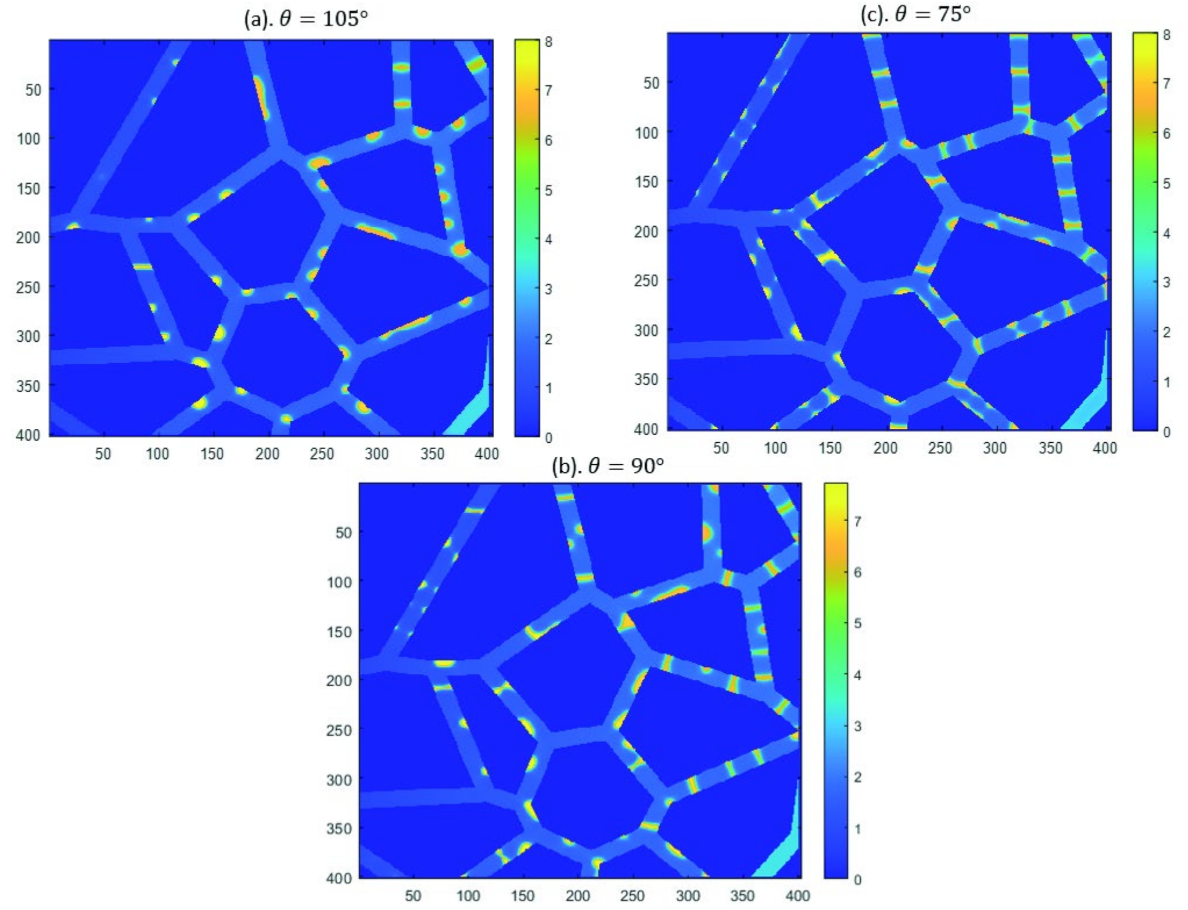

Figure 9: Density distribution of simulated fluid in VT porous media of different wettability conditions. Yellow denotes the condensate liquid. The oil phase is more mobile when theta increases from **(a).** $\boldsymbol{\theta = 75°}$ wetting condition; **(b)** $\boldsymbol{\theta = 90°}$ neutral; **(c)** $\boldsymbol{\theta = 105}$ non-wetting condition.

wettability shifts toward gas-wet, the structure surfaces are less attracted to the liquids, resulting in smaller-sized droplets and films that attach to the structure surfaces. In addition, the liquids tended to flow more easily. **Figure 8** shows the pressure fields during the simulations under different wettability conditions. A clear pressure drop can be observed as the flow goes toward the left, and at the outlets, the reduced pressure, P_r, is approximately 0.5 to 0.6. The bottom sections of the domain have lower pressure due to their higher channel connectivity. For different wettability conditions, the states of condensation and flow differ. In a liquid-wet capillary, films of liquids are formed and are more likely to attach to pore walls, while in a gas-wet capillary, liquids tend to first drop out at the center of capillaries and then gather in rounded globules, droplets, or slugs attached to the structure matrix. **Figure 9** shows a direct comparison of the phase distributions for different wettability conditions in the last frame of the simulation.

Figure 10 and **Figure 11** show the corresponding condensate saturation versus time and saturation versus average domain pressure plots, respectively, for the three different wettability conditions in the VT porous medium. The saturation curves exhibited a clear trend of retrograde condensation, where the condensate accumulated, reached a maximum, and then decreased. The maximum condensate saturation predicted by thermodynamics at equilibrium at T = 530°R (0.140, mole fraction) is included for comparison. The condensate saturation peaks at approximately 14% to 15% at approximately 50,000 ts, which is very close to or slightly above this value because of the influence of the porous media structure surface and flow dynamics. The results also indicate that the liquid-wet porous medium exhibits the highest condensate dropout, while the gas-wet medium shows the lowest. This is likely due to the differences in the wetting characteristics of the porous medium, which affect the distribution of the fluid phases and the accumulation of the condensate.

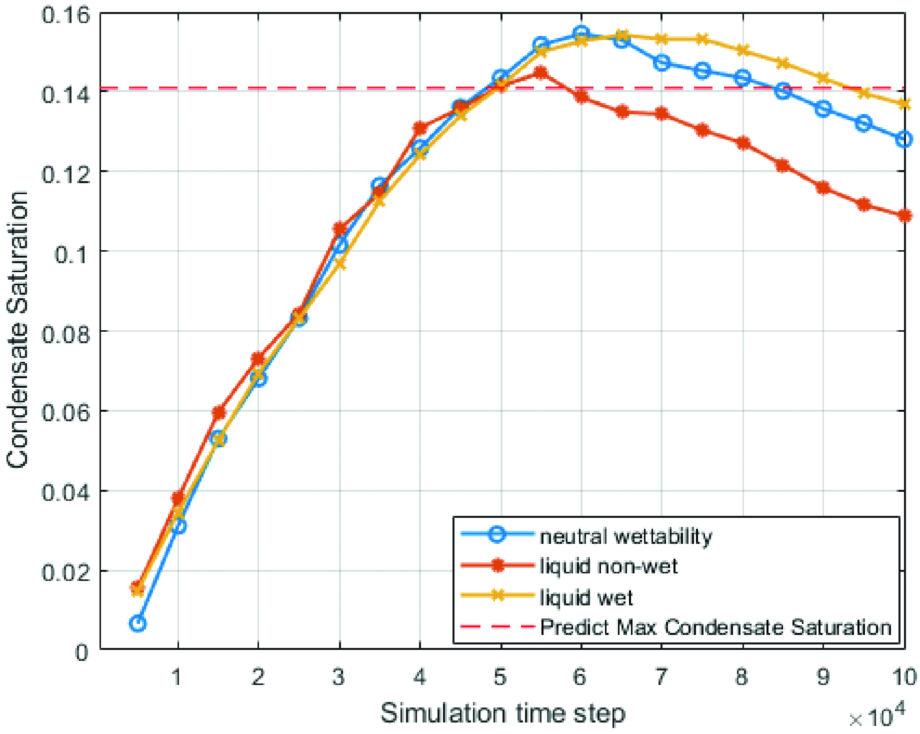

Figure 10: Condensate saturation versus simulation time at different wettability conditions (neutral, liquid non-wet, and liquid wet) in the VT porous medium. According to thermodynamic predictions, the maximum condensate saturation at equilibrium is 0.140.

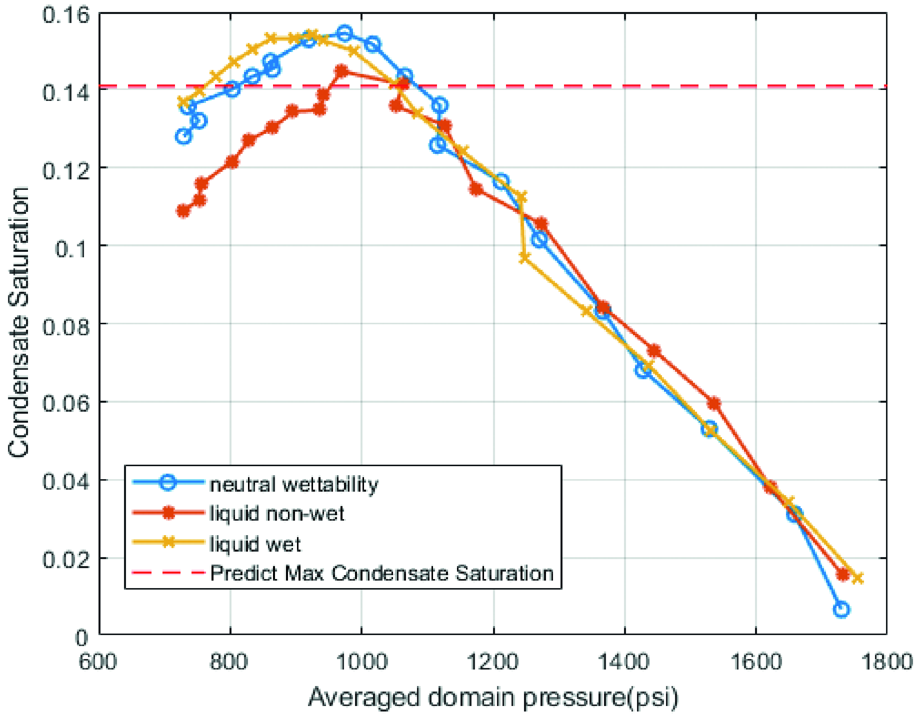

Figure 11: Condensate saturation versus averaged domain pressure at different wettability conditions (neutral, liquid non-wet, and liquid wet) in the VT porous medium. According to thermodynamic predictions, the maximum condensate saturation at equilibrium is 0.140.

4. CONCLUSION

The present study describes a framework for simulating partially miscible MCMP fluids in porous media via the PP LB model. This proposed framework consists of several significant components. The force split scheme based on the PP LB model from a previous study (21) was improved. This model was proven to simulate phase behavior consistent with the thermodynamic predictions. Similar to the idea in (21), the Shan-Chen force is distributed nonuniformly to each component via an adequately designed force split coefficient. Cases of single-phase flows can also be combined under such a γ model.

The recently proposed fluid-structure interaction model (20) was selected in this framework. A fluid-structure model case validation using C3+nC5 fluid by utilizing the framework was also conducted. Such validation proves that, first, in the model, only one parameter ψ_w is directly constructed, which allows for effective and straightforward control of wettability. Second, no nonphysical mass transfer layer was observed in the validation simulations, compared to previous works, which also agrees with the results in (20). Lastly, the value of $cos(\theta)$ is proportional to the parameter ϕ_w.

The generation of the VT porous domain was detailed, and the sufficient channel width was determined using two criteria: resolution to resolve the flow and volume occupied by the interface area. For multiphase flow, the channel width should be at least $16\delta x$, and the ratio between interface thicknesses should not exceed 0.2. Furthermore, the consistent LB scaling system for partially miscible MCMP fluids was discussed. In contrast to the conventional practice of relying solely on CT scanner resolution for single-component or immiscible MCMP fluids, we proposed that the scales of length, time, temperature, mass, and amount of substance should be established based on five independent physical variables.

By integrating each component in the framework, a partially miscible MCMP fluid flow (85%C1+15%nC4) was successfully simulated in the VT porous domain. The retrograde condensation phenomena were observed during the dynamic process. As pressure drops, condensate liquids appear. By altering the surface wettability, we yielded simulation results that reflected the changing wettability conditions and multiphase behaviors that reflect the PVT prediction.

This framework provides a platform to further study the retrograde condensation phenomenon of fluids of interest in the proposed porous media, with a rigorous thermodynamics model. The simulation results stand as one of the pioneering efforts to simulate pore-scale multiphase flow, which captures frame-by-frame phase changes in such a porous media setting.

STATEMENTS AND DECLARATIONS

Supplementary Material

See **Appendix A** for information on the "EOS of Partially-Miscible MCMP Fluids", **Appendix B** for information on the "Derivation of the Force-Split Coefficient at Single-Phase Condition", and **Appendix C** for "The Scaling System of MCMP at the Pore Scale via LB model. The Appendices can be downloaded online here.

Acknowledgements

Funding support from the William A. Fustos Family Professorship in Energy and Mineral Engineering at Penn State University is gratefully acknowledged.

Author Contributions

Zhicheng W. Wang: Conceptualization, Methodology, Software, Validation, Writing – original draft. **Cheng Peng:** Conceptualization, Methodology, Writing – review & editing. **Luis F. Ayala:** Writing – review & editing, Supervision. **Seyyed F. Hosseini:** Writing – review & editing.

Conflicts of Interest

The authors declare that they have no known competing financial interests or personal relationships that could have appeared to influence the work reported in this paper.

Data, Code & Protocol Availability

Data will be made available upon request.

ORCID IDs

Zhicheng W. Wang	https://orcid.org/0000-0002-1184-3180
Cheng Peng	https://orcid.org/0000-0001-7652-3658
Luis F. Ayala	https://orcid.org/0000-0002-7119-3781
Seyyed A. Hosseini	https://orcid.org/0000-0002-3344-6274

REFERENCES

1. Bao, J., & Schaefer, L. (2013). Lattice Boltzmann equation model for multicomponent multiphase flow with high density ratios. *Applied Mathematical Modeling*, 37(4), 1860–1871. https://doi.org/10.1016/j.apm.2012.04.048
2. Benzi, R., Biferale, L., Sbragaglia, M., Succi, S., & Toschi, F. (2006). Mesoscopic modeling of a two-phase flow in the presence of boundaries: the contact angle. *Physical Review E* , 74 , 021509. https://doi.org/10.1103/PhysRevE.74.021509
3. Chapman, S., & Cowling, T. G. (1990). *The Mathematical Theory of Non-uniform Gases. An account of the kinetic theory of viscosity, thermal conduction, and diffusion in gases.* 2nd Edn. pp. Ix, 431. 60s. 1952. Cambridge university press.
4. Chen, L., Kang, Q., Tang, Q., Robinson, B. A., He, Y.-L., & Tao, W.-Q. (2015). Pore-scale simulation of multicomponent multiphase reactive transport with dissolution and precipitation. *International Journal of Heat and Mass Transfer*, 85 , 935–949. https://doi.org/10.1016/j.ijheatmasstransfer.2015.02.035
5. Chevron Energy Technology Company, Schembre-McCabe, J., Kamath, J., Chevron Energy Technology Company, Fager, A., Dassault Systèmes, Crouse, B., & Dassault Systèmes. (2020). Estimation of gas-condensate relative permeability using a lattice boltzmann modeling approach. *Petrophysics – The SPWLA Journal of Formation Evaluation and Reservoir Description*, 61(2), 206–216. https://doi.org/10.30632/PJV61N2-2020a6
6. Colosqui, C. E., Kavousanakis, M. E., Papathanasiou, A. G., & Kevrekidis, I. G. (2013). Mesoscopic model for microscale hydrodynamics and interfacial phenomena: Slip, films, and contact-angle hysteresis. *Physical Review E*, 87(1), 013302. https://doi.org/10.1103/PhysRevE.87.013302
7. Danesh, A (Ed). (1998). *PVT and Phase Behaviour of Petroleum Reservoir Fluids* (1st Ed., Vol. 47). Elsevier. Hardback ISBN: 9780444821966; eBook ISBN: 9780080540054.
8. Deng, H., Jiao, K., Hou, Y., Park, J. W., & Du, Q. (2019). A lattice Boltzmann model for multicomponent two-phase gas-liquid flow with realistic fluid properties. *International Journal of Heat and Mass Transfer*, 128, 536–549. https://doi.org/10.1016/j.ijheatmasstransfer.2018.09.019
9. EIA (Aug 2023). Petroleum – U.S. Energy Information Administration. *EPA report on natural gas and gas condensates.* https://www.eia.gov/naturalgas/data.php
10. Gong, S., & Cheng, P. (2012). Numerical investigation of droplet motion and coalescence by an improved lattice Boltzmann model for phase transitions and multiphase flows. *Computers & Fluids*, 53, 93–104. https://doi.org/10.1016/j.compfluid.2011.09.013
11. Huang, H., Li, Z., Liu, S., & Lu, X. (2009). Shan-and-Chen-type multiphase lattice Boltzmann study of viscous coupling effects for two-phase flow in porous media. International Journal for Numerical Methods in Fluids, 61(3), 341–354. https://doi.org/10.1002/fld.1972
12. Huang, H., Sukop, M., & Lu, X. (2015). *Multiphase Lattice Boltzmann Methods: Theory and Application*. John Wiley & Sons. Print ISBN: 9781118971338, Online ISBN: 9781118971451; DOI: https://doi.org/10.1002/9781118971451
13. Jamiolahmady, M., Danesh, A., Tehrani, D., & Duncan, D. (2000). A Mechanistic Model of Gas-Condensate Flow in Pores. Transport in Porous Media, 41 , 17–46. https://doi.org/10.1023/A:1006645515791
14. Kamali, M. R., & Van Den Akker, H. E. A. (2013). Simulating gas–liquid flows by means of a pseudopotential lattice boltzmann method. *Industrial & Engineering Chemistry Research*, 52(33), 11365–11377. https://doi.org/10.1021/ie303356u
15. Krüger, T., Kusumaatmaja, H., Kuzmin, A., Shardt, O., Silva, G., & Viggen, E. M. (2017). *The lattice Boltzmann method: Principles and practice.* Springer International Publishing. https://doi.org/10.1007/978-3-319-44649-3

16. Lallemand, P., & Luo, L.-S. (2000). Theory of the lattice Boltzmann method: Dispersion, dissipation, isotropy, Galilean invariance, and stability. *Physical Review E*, 61(6), 6546–6562. https://doi.org/10.1103/PhysRevE.61.6546
17. Li, Q., Yu, Y., & Luo, K. H. (2019). Implementation of contact angles in pseudopotential lattice Boltzmann simulations with curved boundaries. *Physical Review E*, 100(5), 053313. https://doi.org/10.1103/PhysRevE.100.053313
18. Martys, N. S., & Chen, H. (1996). Simulation of multicomponent fluids in complex three-dimensional geometries by the lattice Boltzmann method. *Physical Review E*, 53(1), 743–750. https://doi.org/10.1103/PhysRevE.53.743
19. Nilssen, H. N. (2008). Calculation of Interfacial Tension of Methane+ n-Butane Mixture with Gradient Theory Near Critical Conditions. *Preprint submitted to KP8108 – Advanced Thermodynamics*. https://folk.ntnu.no/haugwarb/KP8108/Essays/hui_n_nilssen.pdf
20. Peng, C., Ayala, L. F., & Ayala, O. M. (2021). Fluid-wall interactions in pseudopotential lattice Boltzmann models. *Physical Review E*, 104(3), 035301. https://doi.org/10.1103/PhysRevE.104.035301
21. Peng, C., Ayala, L. F., & Ayala, O. M. (2021). A thermodynamically consistent pseudo-potential lattice Boltzmann model for multicomponent, multiphase, partially miscible mixtures. *Journal of Computational Physics*, 429, 110018. https://doi.org/10.1016/j.jcp.2020.110018
22. Peng, C., Ayala, L. F., Wang, Z., & Ayala, O. M. (2020). Attainment of rigorous thermodynamic consistency and surface tension in single-component pseudopotential lattice Boltzmann models via a customized equation of state. *Physical Review E*, 101(6), 063309. https://doi.org/10.1103/PhysRevE.101.063309
23. Peng, D.-Y., & Robinson, D. B. (1976). A new two-constant equation of state. *Industrial & Engineering Chemistry Fundamentals*, 15(1), 59–64. https://doi.org/10.1021/i160057a011
24. Qian, Y. H., d'Humières, D., & Lallemand, P. (1992). Lattice BGK models for Navier-Stokes equation. *Europhysics Letters*, 17(6), 479. https://doi.org/10.1209/0295-5075/17/6/001
25. Qin, F., Del Carro, L., Mazloomi Moqaddam, A., Kang, Q., Brunschwiler, T., Derome, D., & Carmeliet, J. (2019). Study of non-isothermal liquid evaporation in synthetic micro-pore structures with hybrid lattice Boltzmann model. *Journal of Fluid Mechanics*, 866, 33–60. https://doi.org/10.1017/jfm.2019.69
26. Qin, F., Zhao, J., Kang, Q., Derome, D., & Carmeliet, J. (2021). Lattice boltzmann modeling of drying of porous media considering contact angle hysteresis. *Transport in Porous Media*, 140(1), 395–420. https://doi.org/10.1007/s11242-021-01644-9
27. Qiu, L., Wang, Y., & Reitz, R. D. (2014). On regular and retrograde condensation in multiphase compressible flows. *International Journal of Multiphase Flow*, 64, 85–96. https://doi.org/10.1016/j.ijmultiphaseflow.2014.05.004
28. Shan, X., & Chen, H. (1993). Lattice Boltzmann model for simulating flows with multiple phases and components. *Physical Review E*, 47(3), 1815–1819. https://doi.org/10.1103/PhysRevE.47.1815
29. Shan, X., & Chen, H. (1994). Simulation of nonideal gases and liquid-gas phase transitions by the lattice Boltzmann equation. *Physical Review E*, 49(4), 2941–2948. https://doi.org/10.1103/PhysRevE.49.2941
30. Shan, X., & Doolen, G. (1995). Multicomponent lattice-Boltzmann model with interparticle interaction. *Journal of Statistical Physics*, 81(1–2), 379–393. https://doi.org/10.1007/BF02179985
31. Shardt, N., Wang, Y., Jin, Z., & Elliott, J. A. W. (2021). Surface tension as a function of temperature and composition for a broad range of mixtures. *Chemical Engineering Science*, 230, 116095. https://doi.org/10.1016/j.ces.2020.116095
32. Sigmund, P. M., Dranchuk, P. M., Morrow, N. R., & Purvis, R. A. (1973). Retrograde condensation in porous media. *Society of Petroleum Engineers Journal*, 13(02), 93–104. https://doi.org/10.2118/3476-PA
33. Soleimani, R., Norouzi, S., & Rasaei, M. R. (2019). Investigation of gas condensate drop-out effect on gas relative permeability by Lattice Boltzmann modeling. *The Canadian Journal of Chemical Engineering*, 97(6), 1921–1930. https://doi.org/10.1002/cjce.23442
34. Stiles, C. D., & Xue, Y. (2016). High density ratio lattice Boltzmann method simulations of multicomponent multiphase transport of H2O in air. *Computers & Fluids*, 131, 81–90. https://doi.org/10.1016/j.compfluid.2016.03.003
35. Wang, Z., Soomro, M., Peng, C., Ayala, L. F., & Ayala, O. M. (2022). Two pressure boundary conditions for multicomponent multiphase flow simulations using the pseudo-potential lattice Boltzmann model. *Computers & Fluids*, 248, 105672. https://doi.org/10.1016/j.compfluid.2022.105672
36. Wang, Z. W. (2022). *Pore-Scale Study on Partially Miscible Multiphase Transport in Hydrocarbon Reservoirs Using the Lattice Boltzmann Method* [Ph.D. Thesis, The Pennsylvania State University]. https://etda.libraries.psu.edu/catalog/22154zxw161

37. Welch, W. R. W., & Piri, M. (2015). Molecular dynamics simulations of retrograde condensation in narrow oil-wet nanopores. *The Journal of Physical Chemistry C*, 119(18), 10040–10047. https://doi.org/10.1021/jp511125e
38. Xiao, F. (2013). *Pore-scale simulation frameworks for flow and transport in complex porous media* [Ph.D. Thesis, Colorado School of Mines]. https://repository.mines.edu/bitstream/handle/11124/80368/Xiao_mines_0052E_10321.pdf?sequence=1&isAllowed=y
39. Yuan, P., & Schaefer, L. (2006). Equations of state in a lattice Boltzmann model. *Physics of Fluids*, 18(4), 042101. https://doi.org/10.1063/1.2187070
40. Zhao, J., Kang, Q., Yao, J., Zhang, L., Li, Z., Yang, Y., & Sun, H. (2018). Lattice Boltzmann simulation of liquid flow in nanoporous media. *International Journal of Heat and Mass Transfer*, 125, 1131–1143. https://doi.org/10.1016/j.ijheatmasstransfer.2018.04.123
41. Zhao, J., Yao, J., Zhang, L., Sui, H., & Zhang, M. (2016). Pore-scale simulation of shale gas production considering the adsorption effect. *International Journal of Heat and Mass Transfer*, 103, 1098–1107. https://doi.org/10.1016/j.ijheatmasstransfer.2016.08.026
42. Zheng, J., Chen, Z., Xie, C., Wang, Z., Lei, Z., Ju, Y., & Wang, M. (2018). Characterization of spontaneous imbibition dynamics in irregular channels by mesoscopic modeling. *Computers & Fluids*, 168, 21–31. https://doi.org/10.1016/j.compfluid.2018.01.024